Research Square

Preprints are preliminary reports that have not undergone peer review.
They should not be considered conclusive, used to inform clinical practice,
or referenced by the media as validated information.

A Versatile Four-Channel Plasmonic Demultiplexer Based on Hexagonal Nanocavities Supporting Hybrid Standing-Wave and Traveling-Wave Modes

Ehsan Tahmasbi
Golestan University
Kiazand Fasihi
k.fasihi@gu.ac.ir
Golestan University

Research Article

Keywords: Plasmonics, MIM waveguides, hexagonal nanocavity, standing-wave mode, traveling-wave mode, wavelength-selective reflector, dual-band demultiplexer, coupled mode theory, FDTD

Posted Date: November 12th, 2026

DOI: https://doi.org/10.21203/rs.3.rs-11393094/v1

License: This work is licensed under a Creative Commons Attribution 4.0 International License.
Read Full License

Additional Declarations: No competing interests reported.

Abstract

We propose a compact four-channel wavelength demultiplexer (DEMUX) based on metal-insulator-metal (MIM) plasmonic waveguides side-coupled to hexagonal nanocavities, with identical hexagonal cavities employed as wavelength-selective reflectors. Detailed modal analysis reveals a hybrid behavior: the hexagonal nanocavities support standing-wave resonant modes in the shorter-wavelength Window I (748.55-864.62 nm) and traveling-wave resonant modes in the longer-wavelength Window II (918.22-1065.85 nm) within the same physical structure. For the standing-wave modes, the wavelength-selective reflector significantly enhances the drop efficiency by nearly a factor of two (from ~ 25% to ~ 49%) through destructive interference. Using coupled-mode theory, the optimal reflector distance is derived as $D = \lambda_{spp}/4$ (corresponding to a round-trip phase shift of odd multiples of π). In contrast, the traveling-wave modes exhibit inherently good coupling efficiency (result in a drop efficiency of ~ 33–43% without reflector) and show only a mean marginal improvement of about 5% with the reflector. This modest enhancement is attributed to the interaction of the reflector with a weak standing-wave component that inherently exists in the traveling-wave modes due to the hexagonal geometry. Notably, the traveling-wave regime provides superior channel isolation, with crosstalk values ranging from − 27.2 dB to -48.1 dB across all channels (compared to -14.7 dB to -41.9 dB in the standing-wave regime), making Window II particularly attractive for dense WDM applications. Despite the fundamentally different underlying mechanisms, both bands achieve competitive performance, with peak transmission up to 49.2% and quality factors up to 108. The proposed hybrid modal design provides new physical insights into polygonal plasmonic resonators and offers a versatile platform for dual-band on-chip WDM systems.

1. Introduction

The rapid expansion of data-intensive applications and the emergence of high-speed optical interconnects have created an urgent need for ultra-compact photonic integrated circuits (PICs) capable of handling large bandwidth with minimal footprint and power consumption [1–3]. Traditional dielectric-based photonic devices are fundamentally constrained by the diffraction limit of light, which prevents further miniaturization beyond certain scales. Surface plasmon polaritons (SPPs) propagating at metal-dielectric interfaces provide a powerful solution by enabling strong subwavelength confinement of electromagnetic fields [4–6]. Among different plasmonic waveguide geometries, the metal-insulator-metal (MIM) configuration is particularly attractive for on-chip applications due to its excellent mode confinement, relatively long propagation length, and compatibility with standard nanofabrication processes [7–9].

Wavelength division multiplexing (WDM) is a key technology for increasing data capacity in optical communication systems. Implementing efficient WDM on a chip requires high-performance multiplexers and demultiplexers (MUX/DEMUX) that can combine or separate multiple wavelength channels with low crosstalk, high transmission efficiency, and compact size [10–15]. Over the past decade, various plasmonic MUX/DEMUX structures have been proposed based on directional couplers [16], ring resonators [17], and nanodisk cavities [18–22]. While these designs have shown promising results, they

generally suffer from operation in a single spectral band, moderate transmission efficiencies, and relatively low quality factors. Moreover, many rely on simple broadband metallic mirrors at the end of the bus port, which lack wavelength selectivity and limit further performance optimization.

In this work, we present a four-channel plasmonic DEMUX based on hexagonal nanocavities that exhibits hybrid modal characteristics. Detailed analysis shows that the shorter-wavelength band operates via standing-wave resonances, while the longer-wavelength band is dominated by traveling-wave modes. This distinction has profound implications for the design strategy, particularly regarding the effectiveness of wavelength-selective reflectors. By leveraging both modal types within the same physical layout, the proposed device achieves competitive performance in two distinct near-infrared spectral windows without the need for separate structural re-optimization, offering a versatile solution for multi-standard on-chip WDM systems.

2. Device Structure and Simulation Method

2.1. Device Geometry

Figure 1(a) illustrates the schematic of the proposed four-channel drop-type demultiplexer. The structure consists of a main horizontal MIM bus waveguide and four perpendicular drop waveguides. Each drop waveguide is side-coupled to a main hexagonal nanocavity with side length L_i. At a certain distance from the axis of each drop cavity, another hexagonal nanocavity with the same dimensions is placed as a wavelength-selective reflector. The distance from the beginning of the drop waveguide to the center of the main cavity is denoted d_i, and the distance between the centers of the main cavity and the reflector cavity is denoted D_i.

Fixed parameters include waveguide width W = 50 nm and coupling gap g = 20 nm. Silver is modeled using the Drude dispersion with $\varepsilon_\infty = 3.7$, $\omega_p = 0.38\times10^{16}$ rad/s, and $\gamma = 2.73\times10^{13}$ rad/s. The dielectric regions are air (n = 1). The optimized geometric parameters (L_i, d_i, D_i) and corresponding performance metrics are summarized in Table 1.

Table 1
Optimized geometric parameters and performance metrics of the proposed dual-band DEMUX.

Ch.	L_i (nm)	d_i (nm)	D_i (nm)	Window I λ (nm)	T (%)	Q	Window II λ (nm)	T (%)	Q
1	430	895	1490	748.55	49.1	84.5	918.22	41.1	72.3
2	450	705	1490	776.91	49.2	95.2	958.52	46.2	85.6
3	480	750	2270	822.97	36.3	87.5	1015.49	32.0	91.2
4	510	695	1670	864.62	45.7	108.1	1065.85	35.8	94.7

2.2. Numerical Method

All simulations were carried out using the two-dimensional finite-difference time-domain (2D-FDTD) method. A uniform mesh with spatial steps Δx = Δz=5nm was employed, and perfectly matched layers (PML, 8 layers) were used as absorbing boundaries. A TM-polarized Gaussian pulse covering the wavelength range of interest was launched into the input bus waveguide. Power monitors records the transmitted power at each drop port. Transmission is defined as $T=P_{out}/ P_{in}$, and crosstalk as $10\log_{10}(P_{unwanted}/P_{target})$ evaluated at each resonance wavelength.

3. Results and Discussion

3.1. Dual-Band Demultiplexing Operation

Figure 1(b) presents the normalized transmission spectra at the four drop ports, clearly revealing two distinct and well-separated operational spectral windows. Window I spans the shorter wavelengths (748.55-864.62 nm), while Window II covers the longer wavelengths (918.22-1065.85 nm). Although both bands ultimately achieve comparable transmission levels, their underlying modal physics are fundamentally different, as analyzed in the following sub sections.

3.2. Modal Analysis: Standing-Wave vs. Traveling-Wave Modes

To elucidate the origin of the dual-band behavior, the steady-state magnetic field distributions ($|H_y|$) were examined at representative resonance wavelengths.

In Window I (e.g., λ = 776.91 nm for Channel 1), the field pattern inside the hexagonal cavity exhibits a distinct hexagonal-pole standing-wave distribution, characteristic of Fabry-Perot-like resonance formed by the superposition of waves propagating in opposite directions (see Fig. 2 (a)). This results in strong field confinement and higher quality factors.

In contrast, in Window II (e.g., λ = 958.52 nm), the magnetic field shows a traveling-wave character, with energy circulating along the perimeter of the hexagonal cavity in a whispering-gallery-like manner (see Fig. 2 (b)). This propagating nature leads to relatively weaker confinement compared to the standing-wave modes.

The dual-band behavior thus originates from the hexagonal geometry, which supports a hybrid combination of standing-wave modes in Window I and traveling-wave modes in Window II within the same physical structure. This distinction has significant implications for the role and effectiveness of the wavelength-selective reflector.

3.3. Theoretical Analysis: Coupled Mode Theory for Standing-Wave Modes (Window I)

For the standing-wave modes in Window I, the wavelength-selective reflector plays a critical role in performance enhancement. Employing coupled-mode theory, the round-trip phase shift accumulated by the wave traveling between the main cavity and the reflector cavity is given by $\phi = 2\beta D_i$. Maximum drop efficiency is achieved when the wave returning from the reflector destructively interferes with the directly transmitted wave in the bus waveguide, thereby forcing the optical power into the drop port. This condition requires a total phase shift of $\phi=(2m + 1)\pi$ (odd multiples of π) [23, 24]. Solving for D_i yields the compact design rule $D_i=(2m + 1)\lambda_{spp}/4$. For maximum compactness, we select m = 0, resulting in $D_i = \lambda_{spp}/4$.

Application of this optimized reflector nearly doubles the transmission efficiency in Window I (from approximately 25% without the reflector to ~ 49% with it). The exact values of D_i reported in Table 1 were obtained by fine-tuning this theoretical initial estimate through FDTD parametric sweeps.

3.4. Behavior of Traveling-Wave Modes (Window II)

In contrast to Window I, the resonances in Window II are primarily traveling-wave in nature. A pure traveling-wave mode circulates within the cavity perimeter and couples power into the drop waveguide continuously; therefore, its drop efficiency should be intrinsically independent of any termination at the end of the drop waveguide. However, our simulations reveal a marginal but consistent improvement of approximately 5% when the wavelength-selective reflector is present (e.g., Channel 1 improves from ~ 37.5% to 41.1%, as shown in Fig. 1 (b); similar trends are observed for other channels).

This observation can be well explained by the presence of a weak residual standing-wave component within the otherwise traveling-wave modes. In realistic polygonal cavities, pure traveling-wave circulation is slightly perturbed by partial back-scattering and reflections at the flat facets and coupling gaps of the hexagonal geometry. This scattering excites a minor standing-wave field component that coexists with the dominant traveling wave. Because this residual standing-wave component carries only a small fraction of the total field energy, its resonance exhibits low finesse (broad spectral linewidth) and a correspondingly low Q-factor. Consequently, the dependence of this residual component on the precise reflector distance D_i becomes highly broadband.

This broadband dependence means that a wide range of D_i values will yield a similar marginal enhancement for the residual standing-wave component. Therefore, the specific D_i values rigorously optimized for the dominant standing-wave modes of Window I naturally fall within this permissive range for Window II. This explains why the device exhibits robust dual-band performance without requiring separate, independent optimization of the reflector distances for the two distinct modal regimes.

3.5. Effect of the distance between the cavity center and the beginning of the drop waveguide (d_i) on transmission

Before adding wavelength selective reflectors, the d_i distances were individually optimized via parametric sweeps to maximize power transfer from the bus to the drop port. The simulation results

confirm that the values listed in Table 1 for d_i provide optimal coupling (between the drop cavity and drop port), independent of the modal regime. This robustness eliminates the need for separate d_i optimization for each band.

3.6. Quality Factor and Crosstalk

Window I exhibits higher quality factors (Q_1 = 84.48, Q_2 = 95.20, Q_3 = 87.45, Q_4=108.07), consistent with the stronger field confinement of standing-wave modes. Window II shows slightly lower but still acceptable Q-factors (Q_5 = 72.30 to Q_8 = 94.70). The simulated crosstalk curves for both bands are shown in Fig. 3, and the results are summarized in Table 2. In Window I, crosstalk ranges from − 14.7 dB to -41.9 dB, while in Window II it ranges from − 27.2 dB to -48.1 dB. Notably, Window II exhibits consistently lower crosstalk than Window I for all channels, with the worst-case crosstalk in Window II (-27.2 dB for Channel 3) being significantly better than the worst-case in Window I (-14.7 dB for the same channel). This improved isolation in the traveling-wave regime is attributed to the reduced coupling between adjacent drop waveguides when the energy is circulating rather than forming a standing-wave pattern. Both bands provide adequate channel isolation for on-chip WDM applications, with crosstalk values well below the typical acceptable threshold of -20 dB in most channels.

Table 2
The simulated crosstalk values for Window I and Window II.

Channel	Crosstalk in Window I (dB)	Crosstalk in Window II (dB)
1	-31.6	-31.5
2	-41.9	-48.1
3	-14.7	-27.2
4	-20.9	-27.9

3.7. Add-Multiplexer Configuration

Due to the reciprocity of Maxwell's equations, the same structure functions as an add-multiplexer when the input and output ports are interchanged. Simulations confirm that the add efficiencies are consistent with the drop performance, reaching approximately 50% in Window I and 42% in Window II. The transmission spectra (not shown for brevity) are nearly identical to those presented in Fig. 1(b), as expected from the reciprocity of the linear system. This bidirectional capability further enhances the versatility of the proposed device for on-chip WDM application

3.8. Performance Comparison and Design Insights

Table 3 summarizes the key differences between the two bands. The hybrid modal design successfully leverages the strengths of both standing-wave and traveling-wave resonances, resulting in competitive and balanced performance across both spectral windows without requiring separate structural

optimization. A notable design advantage is that the reflector distances D_i optimized for Window I do not need to be changed for Window II, thanks to the geometric locking of λ_{spp}.

Table 3
Comparison of modal characteristics and design implications.

Feature	Window I (Standing-wave)	Window II (Traveling-wave)
Field pattern	Stationary nodes/antinodes	Propagating along perimeter
Reflector effect	Strong (~ 100% improvement)	Marginal (~ 5% improvement)
Optimal D_i optimization	Critical ($D_i = \lambda_{spp}/4$)	Not critical
Base transmission (no reflector)	~ 25%	~ 33–43%
Final transmission (with reflector)	~ 49%	~ 33–47%
Typical Q-factor	84–108	72–95
Design strategy	Interference-based enhancement	Intrinsic efficiency+weak standing-wave component
Distance re-optimization needed	Yes (for each channel)	Not required (broadband response due to weak residual standing-wave component)

4. Conclusion

We have numerically demonstrated a four-channel plasmonic wavelength demultiplexer based on hexagonal nanocavities that operates through hybrid modal mechanisms: standing-wave resonances in the shorter-wavelength band (Window I) and traveling-wave resonances in the longer-wavelength band (Window II). This physical distinction dictates the optimization strategy; wavelength-selective reflectors are highly effective for standing-wave modes via destructive interference, with the optimal distance derived as $D_i = \lambda_{spp}/4$. In contrast, traveling-wave modes are inherently efficient and benefit only modestly (about 5% improvement) from the reflector.

A key practical advantage is that the reflector distances D_i optimized for Window I remain effective for Window II without modification. This robustness arises because the traveling-wave modes in Window II are largely insensitive to the exact placement of the reflector, due to the weak residual standing-wave component and its associated broadband phase-matching condition (as discussed in Section 3.4). Consequently, the same physical layout that maximizes the standing-wave enhancement in Window I also provides the marginal improvement observed in Window II, eliminating the need for separate optimization of the reflector positions for each band.

Another important finding is that the traveling-wave regime (Window II) exhibits significantly better crosstalk performance compared to the standing-wave regime (Window I). While Window I provides crosstalk values ranging from − 14.7 dB to -41.9 dB, Window II achieves consistently lower crosstalk, ranging from − 27.2 dB to -48.1 dB. This improved isolation in the traveling-wave regime is attributed to the reduced coupling between adjacent drop waveguides when the energy is circulating rather than forming a standing-wave pattern. The worst-case crosstalk in Window II (-27.2 dB for Channel 3) is substantially better than the worst-case in Window I (-14.7 dB for the same channel), making Window II particularly suitable for high-density WDM systems where channel isolation is critical.

The proposed device achieves competitive transmission efficiencies (up to 49.2%) and quality factors (up to 108) in both bands, offering a versatile building block for dual-band on-chip WDM systems. This work provides important new insights into the modal characteristics of polygonal plasmonic resonators and demonstrates a practical hybrid design approach that can be extended to other plasmonic filtering and multiplexing applications.

Declarations

Competing interests

The authors have no relevant financial or non-financial interests to disclose. The authors declare that they have no competing interests.

Funding

The authors did not receive any specific grant from funding agencies in the public, commercial, or not-for-profit sectors. No funding was received to assist with the preparation of this manuscript.

Author Contribution

E. Tahmasbi: Visualization, Validation, Software, Resources, Investigation, Formal analysis, Conceptualization. K. Fasihi: Writing-original draft, Validation, Supervision, Resources, Methodology, Software, Investigation, Formal analysis, Conceptualization.

Acknowledgements

The authors would like to thank Golestan University for providing the research facilities and academic support. During the preparation of this manuscript, a large language model (GPT-4-based) was used solely for language refinement and readability improvement. All technical content, simulations, data analysis, and scientific conclusions are the sole work of the authors. The authors assume full responsibility for the integrity and originality of the work.

Availability of data and material

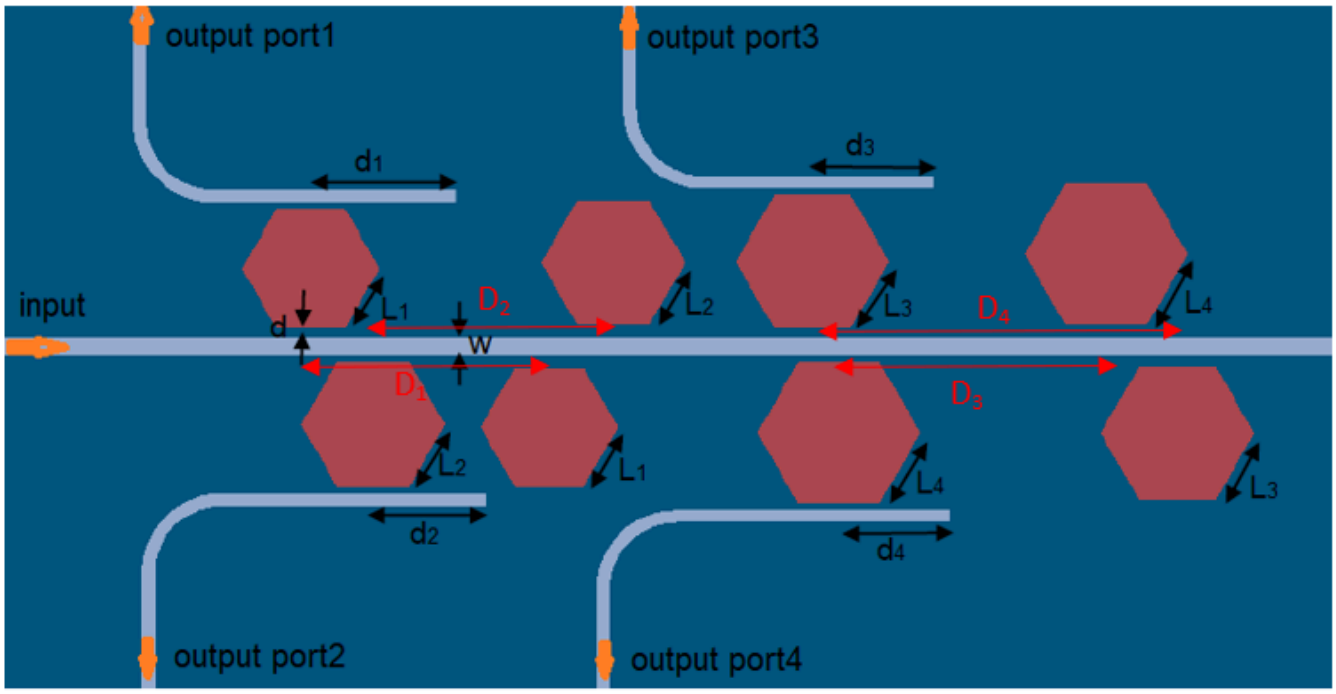
The datasets generated during and/or analyzed during the current study are available from the corresponding author on reasonable request. The Ansys Lumerical simulation files and material parameters used in this work are available from the corresponding author upon reasonable request.

References

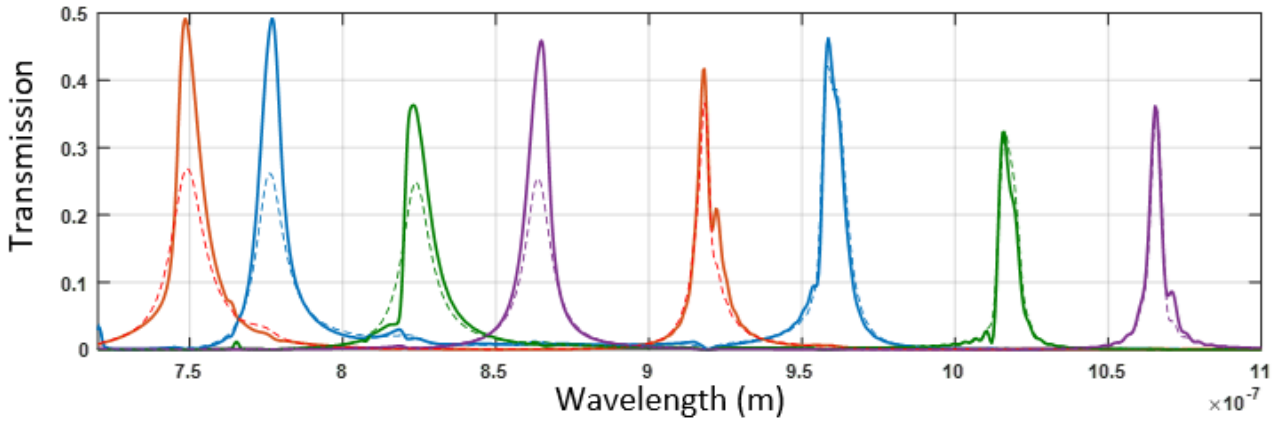
1. Maier, S. A., Plasmonics: Fundamentals and Applications, Springer, 2007.
2. Atwater, H. A. (2007). The promise of plasmonics. Scientific American, 296(4), 56–63.
3. Kazanskiy, N. L., Khonina, S. N., Butt, M. A., Kaźmierczak, A., & Piramidowicz, R. (2021). State-of-the-art optical devices for biomedical sensing applications-A review. Electronics, 10(8), 973.
4. Wang, T. B., Wen, X. W., Yin, C. P., & Wang, H. Z. (2009). The transmission characteristics of surface plasmon polaritons in ring resonator. Optics express, 17(26), 24096–24101.
5. Zia, R., Schuller, J. A., Chandran, A., & Brongersma, M. L. (2006). Plasmonics: the next chip-scale technology. Materials today, 9(7–8), 20–27.
6. Barnes, W. L., Dereux, A., & Ebbesen, T. W. (2003). Surface plasmon subwavelength optics. nature, 424(6950), 824–830.
7. Conway, J. A., Sahni, S., & Szkopek, T. (2007). Plasmonic interconnects versus conventional interconnects: a comparison of latency, crosstalk and energy costs. Optics express, 15(8), 4474–4484.
8. Hosseini, A., & Massoud, Y. (2007, August). A rectangular metal-insulator-metal based nanoscale plasmonic resonator. In 2007 7th IEEE Conference on Nanotechnology (IEEE NANO) (pp. 81–84). IEEE.
9. Wang, G., Lu, H., Liu, X., Mao, D., & Duan, L. (2011). Tunable multi-channel wavelength demultiplexer based on MIM plasmonic nanodisk resonators at telecommunication regime. Optics Express, 19(4), 3513–3518.
10. Khani, S., Danaie, M., & Rezaei, P. (2018). Realization of single-mode plasmonic bandpass filters using improved nanodisk resonators. Optics Communications, 420, 147–156.
11. Hasan, M., Mayoa, F., Hossain, M. S., Ahmed, R., Hossain, M., Ali, K., & Islam, S. (2020). Plasmonic corrugated waveguide coupled to a rectangular nano-resonator as an optical filter. OSA Continuum, 3(12), 3314–3323.
12. Mansuri, M., Mir, A., & Farmani, A. (2021). A tunable nonlinear plasmonic multiplexer/demultiplexer device based on nanoscale ring resonators. Photonic Network Communications, 42(3), 209–218.
13. Nakayama, K., Tonooka, Y., Ota, M., Ishii, Y., & Fukuda, M. (2018). Passive plasmonic demultiplexers using multimode interference. Journal of Lightwave Technology, 36(10), 1979–1984.
14. Nozhat, N., & Granpayeh, N. (2011). Analysis of the plasmonic power splitter and MUX/DEMUX suitable for photonic integrated circuits. Optics Communications, 284(13), 3449–3455.

15. Kang, Z., & Wang, G. P. (2008). Coupled metal gap waveguides as plasmonic wavelength sorters. Optics Express, 16(11), 7680–7685.
16. Han, Z., Liu, L., & Forsberg, E. (2006). Ultra-compact directional couplers and Mach–Zehnder interferometers employing surface plasmon polaritons. Optics communications, 259(2), 690–695.
17. Shafagh, S. G., & Kaatuzian, H. (2024). Ultra-high-sensitive plasmonic sensor based on asymmetric hexagonal nano-ring resonator for cancer detection. Heliyon, 10(14).
18. Lu, H., Liu, X., Mao, D., Wang, L., & Gong, Y. (2010). Tunable band-pass plasmonic waveguide filters with nanodisk resonators. Optics Express, 18(17), 17922–17927.
19. Wu, T., & Cao, W. (2016). A multifunction filter based on plasmonic waveguide with double-nanodisk-shaped resonators. Optik, 127(20), 8976–8982.
20. Mohammadi, M., Soroosh, M., Farmani, A., & Ajabi, S. (2023). Engineered FWHM enhancement in plasmonic nanoresonators for multiplexer/demultiplexer in visible and NIR range. Optik, 274, 170583.
21. Korkmaz, S. (2026). Highly tunable multi-channel metal-insulator-metal waveguide-based wavelength demultiplexers for optical communications. Physica Scripta, 101(19), 195504.
22. SoltaniSarvestani, R., Ghayour, R., & Mohitpour, M. (2025). Design and analysis of an optical demultiplexer based on Bragg grating using plasmonic waveguides and defects. Optik, 322, 172209.
23. Ren, H., Jiang, C., Hu, W., Gao, M., & Wang, J. (2006). Photonic crystal channel drop filter with a wavelength-selective reflection micro-cavity. *Optics Express*, *14*(6), 2446–2458.
24. Fasihi, K., & Mohammadnejad, S. (2009). Highly efficient channel-drop filter with a coupled cavity-based wavelength-selective reflection feedback. *Optics express*, *17*(11), 8983–8997.

Figures



(a)



(b)

Figure 1

(a) Schematic of the proposed four-channel DEMUX with main cavities, the distance from the beginning of the drop waveguide to the center of the main cavity *d*, and reflector cavities separated by *D*. (b) Simulated transmission spectra showing two independent bands. Solid and dashed curves represent the structures with and without wavelength-selective reflectors, respectively.

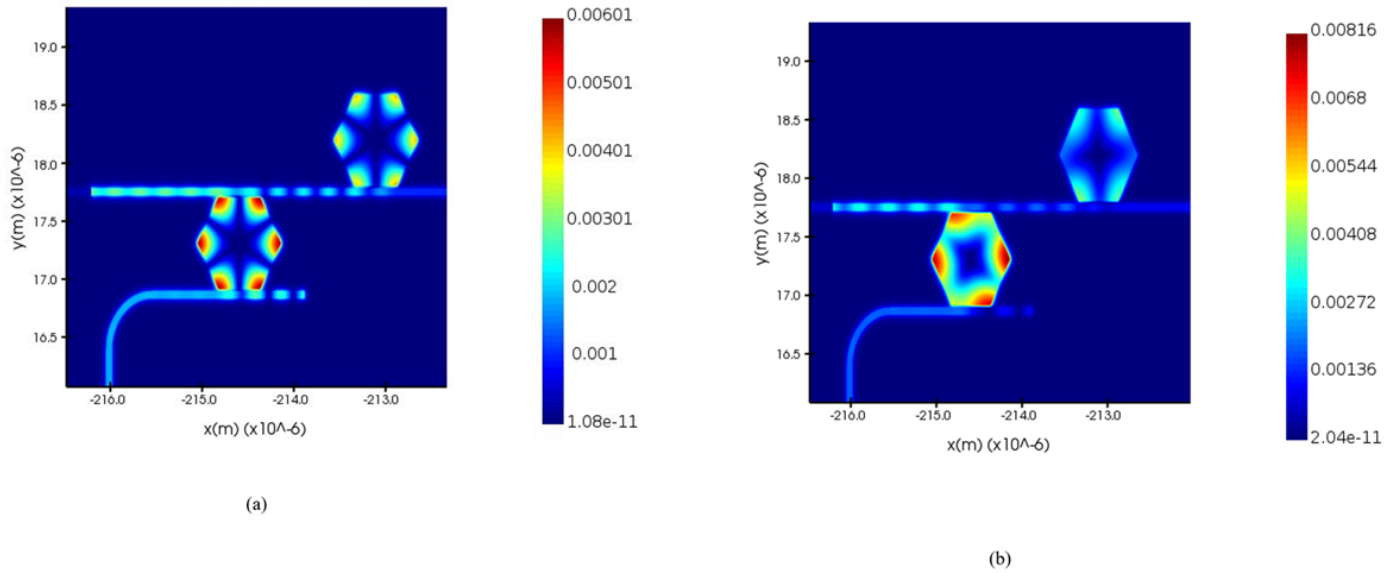


Figure 2

Magnetic field distribution (|Hy|) for channel 2: (a) at 776.91 nm (Window I, standing-wave mode with six-lobe pattern), (b) at 958.52 nm (Window II, traveling-wave mode with quadrupole circulating pattern). The distinct field profiles confirm the different modal nature of the two bands.

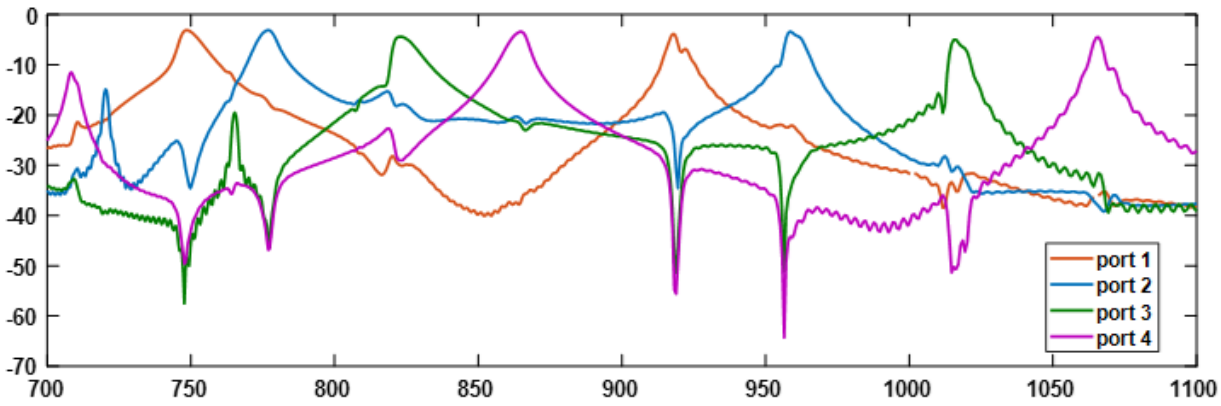


Figure 3

Simulated crosstalk spectra in both bands.